

Chapter VII. Annular Geometry

7.1 Introduction and Motivation

Environmental applications in porous media are mostly characterized by electroosmosis and electromigration as driving mechanisms. For simplicity, the way in which these mechanisms collaborate with other driving forces, i.e. buoyancy and hydrodynamics, has been either ignored or neglected as it is a usual rule of thumb in chemical processes. The characteristic of soil, i.e. heterogeneous, anisotropic, low-permeability, etc., calls for a different approach where the competition among buoyancy, hydrodynamics and electroosmosis/electromigration cannot be overlooked because it may promote distinct flow regimes and, therefore, affect solute transport.

In effect, using rectangular and cylindrical geometries for a capillary channel, it has been previously demonstrated that distinct flow regimes take place under typical electroremediation conditions. Although the objectives of these works have been rather modest, considering the limitation of rectangular and cylindrical systems, the use of both geometries has revealed interesting hydrodynamics aspects to be considered in the design and operation of electrokinetic processes. The mentioned geometries, although useful in the intended study, cannot clearly describe other related hydrodynamic aspects and therefore a different approach is needed. These findings justify the continuation of a similar study in an annular representation of a porous media. The author is perfectly aware that no single geometry can completely described field conditions; however, there are further aspects not yet considered that can be studied by adopting this proposed geometry. In fact, this approximation is more realistic for a porous media than a rectangular or cylindrical geometry in that it provides additional space for the analysis of the effects of porosity and resistive heating of the core on the hydrodynamics of the system. Consequently, this chapter concentrates on

developing the respective annular model and seeks the understanding of the different flow regimes that may be possible in an annular channel.

The present chapter follows closely the systematic analysis of the different effects and parameter ranges presented in Chapters V and VI. Furthermore, this chapter focuses on the analysis of the combined influence of Joule and resistive heating generation with electroosmosis under the action of a pressure gradient. The analysis is based on the application of the fundamental equations of electrokinetic transport to determine *a priori* design criteria and apply these to show the effect of key parameters in controlling flow behavior. The objective here, as in the previous mentioned chapters, is the understanding of the different flow regimes that may be possible in an annular capillary channel.

7.2 Model Formulation

Consider the system been analyzed an annular channel of length L , inner radius R_1 , outer radius R_2 , and an inclination of an angle α with respect to the horizontal line (Figure 7.1). The annular channel is exposed to a constant electrical field E . The inner and outer walls of the channel have nets but constant and uniform charges, Ψ_1^* and Ψ_2^* respectively. The notation $\psi(\xi)$, in figure 7.1, is used to indicate the electrostatic potential across the radial domain of the channel. The outer wall surface presents uniform temperature as defined by it interaction with the temperature of the surroundings T_∞ . The axes (r and x) have been placed coincidentally with the lower end of the capillary channel, x , and the origin of the r -axis at the center of channel. This choice of the coordinate axis is the normal convention in cylindrical coordinates.

The system being modeled requires to us consider at least three main aspects of transport phenomena for the proposed analysis, i.e., heat transfer, electrostatics, and hydrodynamics. From the respective transport equations, profiles of temperature and axial velocity will be obtained for the study of the system behavior. In the sections below, the description of these different aspects is included.

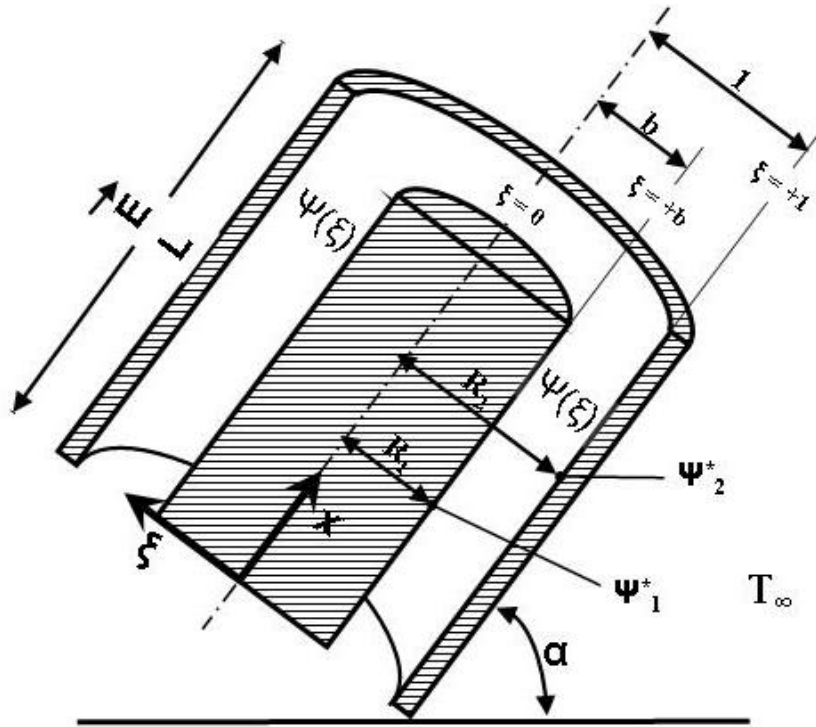


Figure 7.1 Geometrical sketch of the annular capillary channel and coordinate system used in the analysis.

In terms of modeling, only the heat transfer and hydrodynamics of the system will be developed. As indicated in previous chapters, the electrostatic model was widely discussed in Part II for the annular geometry.

7.2.1 Heat Transfer Model

The annular channel (see Figure 7.1) is assumed to interchange heat with its surroundings within a range of efficiencies, i.e., the Nusselt number may take values within a wide spectrum of possibilities. This situation may also lead to the situation in which the temperature of the outer wall surface of the annular channel at the position $r = R_2$ ($\xi = 1$) reach the value of temperature of its environment T_∞ ; this values is considered to be constant. In addition, the ratio R_2/L is assumed small enough to neglect any end effects on the

temperature profile inside the channel. Furthermore, the conduction-dominated regime (Batchelor, 1954) is assumed valid for the present analysis. An applied electrical field E in the axial direction (i.e., the x -axis) of the channel is present and due to the fact that the fluid inside the annular channel and the core show a non-zero resistance to the electrical current, heat generation takes place. For this study the generated heat is assumed constant with time and uniform across the annular channel. This situation yields two cases of heat transfer that need to be analyzed separately; this is the heat generation in the core and in the fluid.

The analysis of the core presents similarities with the electric heating of a wire for which Bird et al. (1960) demonstrated its modeling. In this case, the wire is the core of the annular channel. By applying Fourier's law the following equation is obtained:

$$-\frac{\partial \theta}{\partial \xi} = \phi_e^2 \xi \quad (7.1)$$

The following definitions have been used for the non-dimensional expressions:

$$\xi \equiv \frac{r}{R_2}; \quad \theta \equiv \frac{(T - T_\infty)}{T_\infty}; \quad \phi_e^2 \equiv \frac{S_e R_2^2}{2 K_C T_\infty} \quad (7.2)$$

where, ϕ_e^2 is the resistive heating number, S_e the heat generation rate per volume unit, K_C the thermal conductivity of the core of the annular channel, and T_∞ the ambient temperature, beyond $r = R_2$ ($\xi = 1$).

Equation 7.1 can be easily solved assuming that K_C is constant and using the boundary condition

$$\theta \Big|_{\xi=b} = \theta(b) \quad @ \quad \xi = b \quad (7.3)$$

In the fluid part of the system, this non-zero resistance to the electrical current is known as the Joule heating effect and, under the assumptions described above; the energy equation (Bird et al., 1960) reduces to:

$$-\frac{1}{\xi} \frac{\partial}{\partial \xi} \left(\xi \frac{\partial \theta}{\partial \xi} \right) \equiv \phi^2 \quad (7.4)$$

In equation 7.4, right hand side, the Joule heating number has been identified as:

$$\phi^2 \equiv \frac{Q R_2^2}{K_F T_\infty} \quad (7.5)$$

where, Q is the Joule heating generation, and K_F the thermal conductivity of the fluid of the annular channel.

The conservation of energy equation 7.4 needs boundary conditions at both the inner wall and the outer wall surface of the annular channel; although different types of boundary conditions are possible (Incropera and De Witt, 1996; Boland et al., 2000) in this analysis the simplest case is used. Therefore, the flux or Robin boundary conditions (Incropera and Witt, 1996) are selected and they are given by the following equations.

$$-\left. \frac{\partial \theta}{\partial \xi} \right|_{\xi=b} = \phi_e^2 \xi \left. \frac{\partial \theta}{\partial \xi} \right|_{\xi=b} \quad @ \quad \xi = b \quad (7.6a)$$

$$-\left. \frac{\partial \theta}{\partial \xi} \right|_{\xi=+1} = Nu \cdot \theta \left. \frac{\partial \theta}{\partial \xi} \right|_{\xi=+1} \quad @ \quad \xi = +1 \quad (7.6b)$$

In the previous expression, equation 7.6b, the Nusselt number, Nu , is defined as

$$\text{Nu} \equiv \frac{h R_2}{K_F} \quad (7.7)$$

where h is the convective coefficient, and all the other parameters have been defined above.

As described above, in terms of heat transfer there are two differential models to be solved. The first one is related to the core of the annular channel represented by equation 7.1 with boundary conditions equation 7.3 a&b. The integrated solution is computed as:

$$\theta(\xi) = \theta(b) + \frac{\phi_c^2 b^2}{2} \left\{ 1 - \left(\frac{\xi}{b} \right)^2 \right\}; \quad 0 \leq \xi \leq b \quad (7.8)$$

The second solution, related to the fluid and described by equation 7.4 with boundary conditions equation 7.6 a&b, is readily computed as:

$$\theta(\xi) = \frac{\phi^2}{4} - \frac{\phi^2}{4} \xi^2 + \left\{ \frac{\phi^2}{2} b^2 - \phi_c^2 b^2 \right\} \ln|\xi| + \frac{1}{\text{Nu}_u} \left\{ \frac{\phi^2}{2} - \frac{\phi^2}{2} b^2 + \phi_c^2 b^2 \right\}; \quad b \leq \xi \leq 1 \quad (7.9)$$

Equation 7.9 is an analytical function of the position of the cylindrical channel, across the radial direction, and it is very useful in the computation of the hydrodynamic velocity profile to be described in a section below. However, some interesting limiting cases can be derived from equation 7.9 when examined. For example, the situation of a high convective cooling system, high Nusselt number values, leads to:

$$\theta(\xi) = \frac{\phi^2}{4} - \frac{\phi^2}{4} \xi^2 + \left\{ \frac{\phi^2}{2} b^2 - \phi_c^2 b^2 \right\} \ln|\xi| \quad (7.8a)$$

and for any Nusselt number value, the minimum temperature is located at the wall surface, location $\xi=1$, which is exposed to ambient temperature T_∞ . This is:

$$\theta(1) = \frac{1}{N_u} \left\{ \frac{\phi^2}{2} - \frac{\phi^2}{2} b^2 + \phi_e^2 b^2 \right\} \quad (7.8b)$$

This situation produces the lowest temperature in the fluid system for any value of the Joule heating parameter, ϕ^2 , and resistive heating number, ϕ_e^2 . Also, the temperature difference between any value and the lowest value is readily given by:

$$\Delta\theta(\xi) = \frac{\phi^2}{4} - \frac{\phi^2}{4} \xi^2 + \left\{ \frac{\phi^2}{2} b^2 - \phi_e^2 b^2 \right\} \ln|\xi| \quad (7.8c)$$

This equation becomes useful to predict temperature differences at any location of the annular channel and the surface of such domain.

7.2.2 Hydrodynamic Model

The fluid in the annular channel, as described above, is assumed to be Newtonian, incompressible for the mass conservation aspects and under steady state conditions. This fluid is also assumed to have constant properties everywhere except for the density in the buoyancy force term. This is, in fact, the assumption suggested by Boussinesq (Gebhart et al., 1988). All the assumptions described for heat transfer are assumed valid for the hydrodynamic flow problem as well. In particular, the “no end effects” and the conduction-dominated regime (i.e., small magnitude of velocity field) are invoked here. Moreover, a pressure gradient is assumed to be present but its magnitude must be relatively small to comply with the assumption of a small velocity field. Under these assumptions, the axial or x-component of the Navier-Stokes equation (Bird et al., 1960) is given by

$$\frac{1}{r} \frac{\partial}{\partial r} \left(r \mu \frac{\partial V_x}{\partial r} \right) = \frac{\partial p}{\partial x} - \rho(T) g_x - \rho_e(\psi) E_x \quad (7.9)$$

where the applied electrical field in the axial direction, E_x , is assumed constant at porosity of 100% (E_{x0} @ $b=0$) but related to the area of the porous, annular area of the channel, according to (Wu and Papadopoulos, 2000)

$$E_x = \frac{E_{x0}}{1-b^2} \quad (7.10a)$$

and the function $\rho(T)$ is computed by a first order Taylor approximation around a mean temperature T_m of the system (Bird et al., 1960)

$$\rho(T) = \rho(T_m) - \beta_m \rho_m (T - T_m) \quad (7.10b)$$

and where β_m is the volumetric compressibility of the fluid at a mean temperature T_m . Now, the parameter T_m is determined by the total mass conservation condition that may be stated as

$$2 \pi \int_{R_1}^{R_2} \rho(T_m) V_x(y, T_m) r dr = 0 \quad (7.11a)$$

or, as a dimensionless equation

$$2 \pi \int_b^1 \rho_m V_x^+(\xi, \theta_m) \xi d\xi = 0 \quad (7.11b)$$

The condition given by equation 7.11 requires the computation of the hydrodynamic velocity profile previously to its solution. Finally, the function ρ_e , electrostatic density, is defined by the following expression

$$\rho_e = -\frac{\varepsilon \cdot k^2}{4 \cdot \pi} \cdot \psi(\xi) \quad (7.12)$$

where ε is the media permittivity and k is inverse of the Debye length.

Equation 7.12 features the electrostatic potential, $\psi(\xi)$, that is obtained by solving the Poisson-Boltzmann equation, simplified by the Debye-Huckel approximation, as it was described in chapter III, and improved using f_{AO} , the correction function method, proposed in chapter IV.

In order to have a convenient way of analyzing the different aspects related to the velocity profile $V_x(r)$, the following dimensionless variables and numbers are proposed.

$$V_E = \frac{E_{x0} \cdot \varepsilon \cdot \psi_2}{4 \cdot \pi \cdot \mu} \quad (7.13a)$$

$$V_x^+ = \frac{V_x}{V_E} \quad (7.13b)$$

$$G_r = \frac{\beta_m \cdot \rho_m^2 \cdot R_2^3 \cdot T_\infty \cdot g}{\mu^2} \quad (7.13c)$$

$$G_r^* = \beta_m \cdot T_\infty \cdot G_r \quad (7.13d)$$

$$R_e = \frac{V_E \cdot R_2 \cdot \rho_m}{\mu} \quad (7.13e)$$

$$P_m = \frac{\partial h_p}{\partial x} \cdot \frac{G_r^*}{R_e} + \sin(\alpha) \cdot \frac{G_r^*}{R_e} \quad (7.13f)$$

The Grashoff numbers, Gr and Gr^* , represent the buoyancy to viscous forces due to changes in temperature and density respectively, while in equation 7.13e, the Reynolds number, Re , represents the inertia to viscous forces. A convenient combination of Grashoff and Reynolds numbers has been mathematically applied to dimensionally reduce the total hydraulic head gradient, which yields the dimensionless number P_m , equation 7.13f. By using these numbers and variables in the Navier-Stokes component, equation 7.10, the following dimensionless differential equation is obtained

$$\frac{1}{\xi} \frac{\partial}{\partial \xi} \left(\xi \frac{\partial V_x^+}{\partial \xi} \right) = P_m - \frac{Gr}{R_e} \cdot \sin(\alpha) \cdot (\theta - \theta_m) + \frac{\lambda^2}{1-b^2} \frac{\psi(\xi)}{\psi_2} \quad (7.14)$$

This equation shows several terms that account for the different forces present in the system. The left side of the equation is the viscous term, the first term on the right side represents the pressure driven force, the second is related to the buoyancy effects, and the last one is associated with the electroosmosis term.

In order to complete the problem for the electro-hydrodynamic velocity profile, the non slip-boundary conditions, at the inner and outer wall surfaces, will be assumed for the annular channel

$$V_x^+ \Big|_{\xi=b} = 0 \quad @ \quad \xi = b \quad (7.15a)$$

$$V_x^+ \Big|_{\xi=1} = 0 \quad @ \quad \xi = 1 \quad (7.15b)$$

Equation 7.14 can be trivially solved by simple substitution of the temperature, $\theta(\xi)$, and electrostatic potential, $\psi(\xi)$, profile equations followed by mathematical integration and constants' evaluation using the boundary conditions of equations 7.15 a&b. The proposed mathematical solution yields:

$$V_x^+(\xi) = \frac{A_0}{4} (\xi^2 - 1) + \frac{A_1}{16} (\xi^4 - 1) - \frac{A_2}{8} (2 \xi^2 \ln|\xi| - \xi^2 + 1) + A_3 \ln|\xi| + \left\{ \frac{1 - \psi^*(\xi)}{1 - b^2} \right\} + \left\{ \frac{\psi_{12} - 1}{1 - b^2} \right\} \frac{\ln|\xi|}{\ln|b|} \quad (7.16)$$

where, the following parameters and expressions have been identified in the function above:

$$A_0 = P_m - \frac{G_r}{R_e} \sin(\alpha) \left[\frac{\phi^2}{4} (1 - b^2) + \frac{\phi_e^2}{2} b + \theta_{\text{MIN}} - \theta_m \right] \quad (7.17a)$$

$$A_1 = \frac{G_r}{R_e} \sin(\alpha) \frac{\phi^2}{4} \quad (7.17b)$$

$$A_2 = \frac{G_r}{R_e} \sin(\alpha) \left(\frac{\phi^2}{2} b^2 - \phi_e^2 b^2 \right) \quad (7.17c)$$

$$A_3 = \left(\frac{A_0}{4} (1 - b^2) + \frac{A_1}{16} (1 - b^4) + \frac{A_2}{8} (2 b^2 \ln|b| - b^2 + 1) \right) \frac{1}{\ln|b|} \quad (7.17d)$$

$$\psi^*(\xi) = \frac{\Psi(\xi)}{\Psi_2} \quad (7.17e)$$

$$\Psi_{12} = \frac{\Psi_1}{\Psi_2} \quad (7.17f)$$

The parameters A_0 and A_2 are closely related to the buoyancy driven term, affected by the Joule and resistive heating effect, and are porosity dependant. Only A_0 is related to the pressure driven term. A_1 is not affected by resistive heating but by buoyancy forces. Finally, A_3 is a combination of the previous parameters and consequently inherits their characteristic driven by porosity. Some of the qualitative and semi-qualitative information about the flow given by the hydrodynamic velocity profile is analyzed in the section below.

7.2.3 The Mass Conservation Condition

As indicated before, equation 7.11, the mass conservation restriction, must be solved to obtain an expression for the system mean temperature, T_m , or its equivalent dimensionless form, θ_m . This step is the mathematical closure procedure to complete the system modeling. The analytical expression derived in this case corresponds to:

$$\theta_m = \frac{C_0 \phi^2 + C_1 \left(\frac{\phi^2}{2} b^2 - \phi_e^2 b^2 \right) - C_2 P_m + C_3 - 16 C_4}{\frac{G_r}{R_e} \sin(\alpha) C_2} + \left[\frac{\phi^2}{4} (1 - b^2) + \frac{\phi_e^2}{2} b + \frac{1}{N_u} \left\{ \frac{\phi^2}{2} - \frac{\phi^2}{2} b^2 + \phi_e^2 b^2 \right\} \right] \quad (7.18)$$

where, the following parameters have been isolated in the function above for presentation purpose.

$$C_0 = \frac{-1 G_r}{48 R_e} \sin(\alpha) (4b^6 \ln|b| + 3b^2 - 3b^6 - 3 + 3b^4 - 4 \ln|b|) \frac{1}{\ln|b|} \quad (7.19a)$$

$$C_1 = \frac{1 G_r}{4 R_e} \sin(\alpha) (4b^4 (\ln|b|)^2 - 5b^4 \ln|b| + 4b^2 \ln|b| + 2b^4 - 4b^2 + 2 + \ln|b|) \frac{1}{\ln|b|} \quad (7.19b)$$

$$C_2 = \{b^4 \ln|b| - b^4 + 2b^2 - 1 - 2 \ln|b|\} \frac{1}{\ln|b|} \quad (7.19c)$$

$$C_3 = \left\{ 2b^2 - 2 + \frac{\Psi_{12} - 1}{\ln|b|} (2b^2 \ln|b| - b^2 + 1) \right\} \frac{4}{1 - b^2} \quad (7.19d)$$

$$C_4 = \left\{ \frac{[I_0(\lambda \cdot b) - \Psi_{12} \cdot I_0(\lambda)] [b K_1(\lambda b) - K_1(\lambda)] + [\Psi_{12} \cdot K_0(\lambda) - K_0(\lambda \cdot b)] [b I_1(\lambda b) - I_1(\lambda)]}{(I_0(\lambda \cdot b) \cdot K_0(\lambda) - I_0(\lambda) \cdot K_0(\lambda \cdot b)) (1 - b^2) \lambda} \right\} \quad (7.19e)$$

In equations 7.18 and 7.19 (a-e), it is observed that the mean temperature term, θ_m , is a linear function of the parameter P_m , the Reynolds number, Re , Joule heating generation, ϕ^2 , and resistive heating generation, ϕ_e^2 . In contrast, θ_m is an hyperbolic function of both the Nusselt, Nu , and the Grashoff number, Gr , as well as of the inclination angle, α . Similarly, the inverse dimensionless Debye length (λ) and the core radius (b) show non-linear relationships with the mean temperature expression.

7.3 Design Criteria

Design criteria must be developed before meaningful numerical values for the temperature and velocity profiles are computed. This task has been successfully accomplished by restricting the range of feasible Joule heating generation number, ϕ^2 , and resistive heating number, ϕ_e^2 , to those values that in combination do not imply a change in the fluid phase. Under ambient conditions change of phase will occur at temperature values of approximately $\theta \geq 0.28$ yielding a range of the Joule heating generation number of $0 \leq \phi^2 \leq 0.9$ and resistive heating number of $0 \leq \phi_e^2 \leq 1.0$. Another physical constraint taken into consideration is that the mean temperature can not exceed the maximum temperature in the system. By using this physical constraint, a range of feasible values for the dimensionless hydraulic head gradient has been derived. In particular, equations 20a and 20b are used to identify the location of maximum temperature and its value respectively. The described criteria are implicit in all the calculation herein presented.

$$\xi_{\text{MAX}} = b \quad (7.20a)$$

$$\theta_{\text{MAX}} = \frac{\phi^2}{4}(1 - b^2) + \left\{ \frac{\phi^2}{2} b^2 - \phi_e^2 b^2 \right\} \ln|b| + \frac{1}{N_u} \left\{ \frac{\phi^2}{2} - \frac{\phi^2}{2} b^2 + \phi_e^2 b^2 \right\} \quad (7.20b)$$

On the other hand, equations 21a and 21b, given below, are used to identify the location of minimum temperature and its value respectively.

$$\xi_{\text{MIN}} = 1 \quad (7.21a)$$

$$\theta_{\text{MIN}} = \frac{1}{N_u} \left\{ \frac{\phi^2}{2} - \frac{\phi^2}{2} b^2 + \phi_e^2 b^2 \right\} \quad (7.21b)$$

By using the expressions for maximum and minimum temperature in the system, equations 7.20b and 7.21b, in combination with the expression for the mean temperature, equation 7.18, the following dimensionless hydraulic head gradient criteria are established.

$$Pm_{\text{MIN}} = \frac{C_0 \phi^2 + C_1 \left(\frac{\phi^2}{2} b^2 - \phi_e^2 b^2 \right) + C_3 - 16 C_4}{C_2} + \frac{G_r}{R_e} \sin(\alpha) \left\{ \frac{\phi_e^2}{2} b^2 - \left(\frac{\phi^2}{2} b^2 - \phi_e^2 b^2 \right) \ln|b| \right\} \quad (7.22)$$

$$Pm_{\text{MAX}} = \frac{C_0 \phi^2 + C_1 \left(\frac{\phi^2}{2} b^2 - \phi_e^2 b^2 \right) + C_3 - 16 C_4}{C_2} + \frac{G_r}{R_e} \sin(\alpha) \left\{ \frac{\phi_e^2}{2} b^2 + \frac{\phi^2}{4} (1 - b^2) \right\} \quad (7.23)$$

The use of these design equations is very useful to identify parameter values for the numerical illustrations that are presented in the next section. Once again, the criteria represented by equations 7.22 and 7.23 are implicit in all the calculations herein presented.

7.4 Illustrative Results and Discussion

This section particularly focuses on the use of the developed criteria (see section 7.3 above) in combination with the model solutions (see section 7.2 above) to obtain the temperature and the hydrodynamics velocity profiles. Several case scenarios of the main system variables have been portrayed for analysis and discussion.

Figure 7.2 (a,b,c&d) and 7.3 (a&b) show the temperature profile for different combination of two cases of resistive heating number (ϕ_e^2), two cases of core radius number (b), and two cases of Nusselt number (Nu) with the Joule heating number, ϕ^2 , as a parameter ranging between the values of 0.05 and 0.90. For cooling system (Nu = 10), figure 7.2 illustrates cases with no resistive heating $\phi_e^2 = 0$, b = 0.2 **(a)** and b=0.4 **(b)**; with resistive

heating $\phi_c^2=0.7$, $b = 0.2$ **(c)** and $b=0.4$ **(d)**. For less cooling system ($Nu = 5$), figure 7.3 shows cases with no resistive heating $\phi_c^2=0$, $b = 0.2$ **(a)** and $b=0.4$ **(b)**. A general view of figure 7.2 suggests that due to the symmetric characteristics of the system, the locations of maximum temperature values are found at the center region of the annular capillary. In addition, an increase in the Joule heating parameter yields a more pronounced parabolic type curve, flattened at the top when no resistive heating occurs. For example at center locations $\xi=0$, an increment of ϕ^2 from 0.25 to 0.70 produces an increase in temperature of approximately 180%. At the same location, an increment of ϕ^2 from 0.25 to 0.50 produces an increase in temperature of approximately 100% and an increment of ϕ^2 from 0.05 to 0.25 increases temperature by 400%. This observed effect indicates that a small variation on the Joule heating parameter may cause an important impact on the system temperature especially in the lower range of ϕ^2 . Now, when comparing figures 7.2a and 7.2b (or 7.3a and 7.3b), it is clearly observed the important role of porosity on temperature development. When the core presents no resistive heating, a lower porosity reduces the effect of joule heating and therefore a flattened at the top temperature profile is developed. On the contrary, when the core does present resistive heating as shown in figure 7.2c and 7.2d, a steeper temperature profile is observed dominated by resistive heating. In this case the effect of a lower porosity amplifies the resistive heating effect just described. Now, comparing figures 7.2a and 7.3a (or 7.2b and 7.3b) the role of the heat exchange forces is clearly working; for example, in the case of the smaller Nusselt values there is a “lifting” effect on all the temperature values, equally distributed along the radial position ξ .

In order to illustrate the role of the Joule heating, resistive heating, porosity, buoyancy, electroosmosis and pressure driven forces on the velocity profile six set of figures are presented and analyzed. On all these plots the inverse dimensionless Debye length is used as a parameter between $\lambda = 1$ and $\lambda= 20$. This particular range covers the most typical values of inverse dimensionless Debye lengths that have actual effect on the electrostatic potential and, therefore, on velocity.

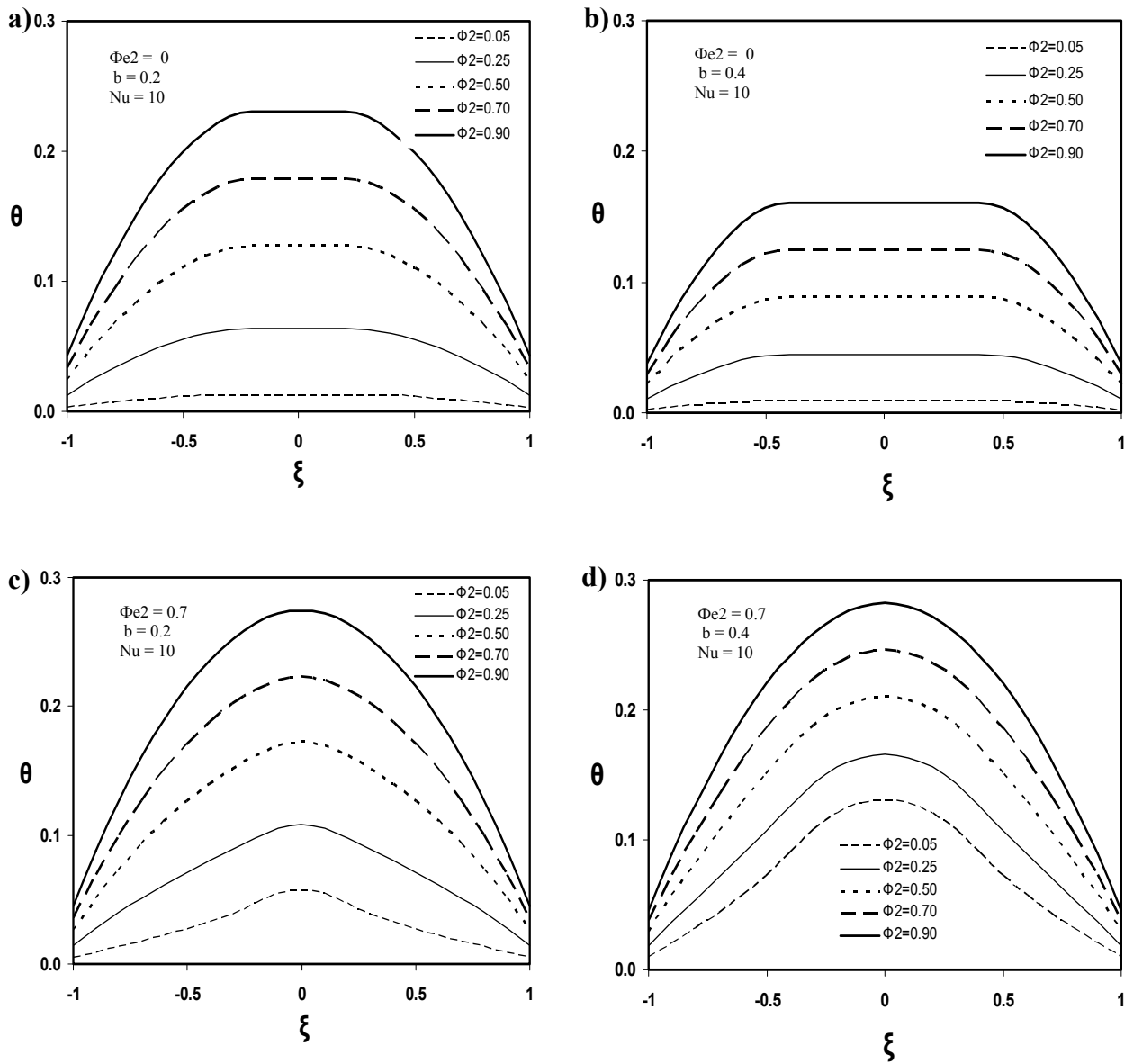


Figure 7.2 Dimensionless temperature profiles (inside the annular capillary channel) for various values of the heat generation parameter and cooling system ($Nu = 10$).

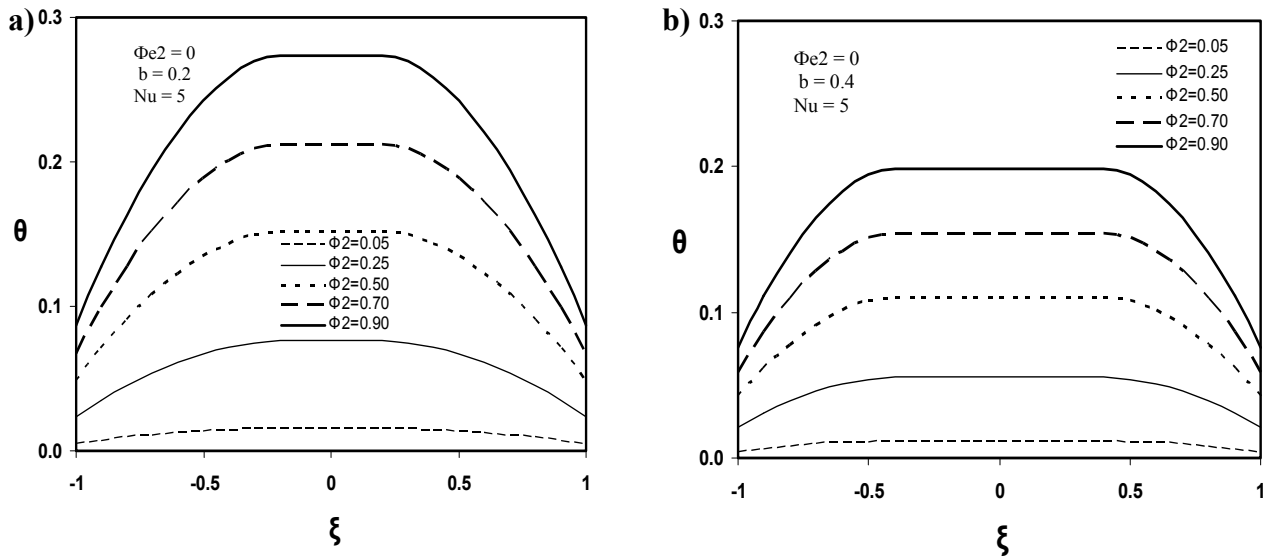


Figure 7.3 Dimensionless temperature profiles (inside the annular capillary channel) for various values of the heat generation parameter and less cooling system ($Nu = 5$).

Figure 7.4 (a,b&c) show velocity profiles for three cases of Joule heating parameter, respectively, with inverse dimensionless Debye length as a parameter. Furthermore, dimensionless-axial velocity profiles (inside the annular capillary channel) are shown for different values of the Joule heating number, $\phi^2 = 0.05$ (a); $\phi^2 = 0.5$ (b); and $\phi^2 = 0.9$ (c). In all the three situations, the dimensionless inverse Debye Hückel length, λ , is used as a parameter with the values indicated in the figure. On this set of plots the Grashoff number, Gr , has been held at the value of unity and the electrical potential ratio, Ψ_{12} , equal to 0.8. In figure 7.4a, it is clearly observed that at low values of ϕ^2 (0.05) electroosmosis dominates controlling the flow for all λ values. In particular, as λ values increase from 1 to 20, the location of maximum punctual velocity moves from a near to the inner wall position to a position near the outer wall. In the next two plots, figure 7.4 (b&c), where the Joule heating parameter is gradually increased, buoyancy forces begin to compete changing the direction of flow at the midway of the annular region. The phenomenon just described causes *flow reversal regime* at higher

magnitude of the inverse dimensionless Debye length, however, this trend tends to disappear at higher Joule heating parameter.

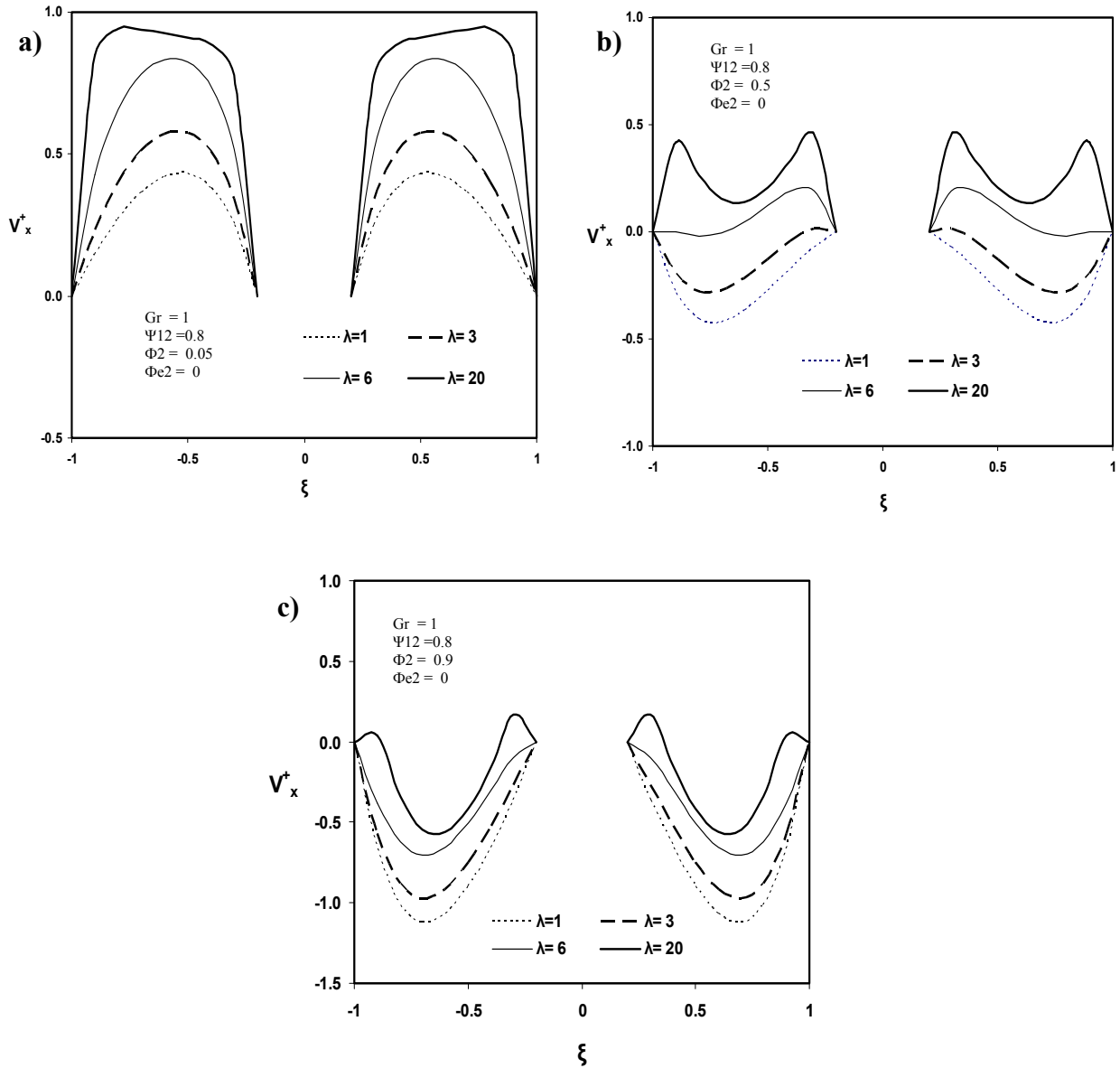


Figure 7.4 Typical hydrodynamic behavior of the physical system for Grashof number $Gr = 1$, electrical field in the axis direction, electrical potential ratio $\Psi_{12} = 0.8$, and no resistive heating effect $\phi_c^2 = 0$.

Figures 7.5 (a,b&c) describe the same variables as in figures 7.4 (a,b&c); however, resistive heating has been introduced and held at the value of unity. In general, the set of figures allows verifying the influence of the heat generation due to electrical resistive of the core. The overall trend is very similar to that of figure 7.4; however, the main difference is that all the locations of maximum punctual velocities have moved to a position near the inner wall. This clearly indicates that buoyancy is responsible force as higher temperature values are developed in the inner wall region.

Figures 7.6 (a,b&c) also illustrate the same variables as in figures 7.4 (a,b&c) however resistive heating has been introduced and held at the value of unity as in figure 7.5 (a,b&c). Additionally, the electrical potential ratio, Ψ_{12} , has been held high (1.8). By stressing this last parameter, in general terms, the moving effect of maximum punctual velocity location to the inner wall is amplified. In this case buoyancy and electroosmotic forces collaborate to produce a “lifting” effect on all the positive velocity values starting at the inner wall and gradually vanishing toward the outer wall. On the contrary, negative velocity values are uniformly amplified yielding a pressure driven type of flow. Overall, the occurrence of *flow reversal regimes* is more evident in figure 7.6 than in the two previous figures. For example, figure 7.6a presents a *flow reversal regime* for $\lambda = 1$ which was not observed before. Additionally, figure 7.6 b&c shows amplified versions of the *flow reversal* identified in figure 7.4 b&c.

Figures 7.7 (a,b&c) illustrate velocity profiles for three cases of Joule heating parameter, respectively, with inverse dimensionless Debye length as a parameter. On this set of plots the Grashoff number, Gr , has been held at the value of unity and the electrical potential ratio, Ψ_{12} , held high (1.8). No resistive heating effect is considered and the porosity has decreased ($b = 0.4$). Comparing figure 7.7 a,b&c for low λ values (< 3), it is clearly observed a gradual reversal of flow toward a fully developed pressure driven flow, as the Joule heating effect increases. However, for high values of λ (≤ 6), a competition between electroosmotic and buoyancy forces gradually develop a *flow reversal regime* that is more evident with high Joule heating values.

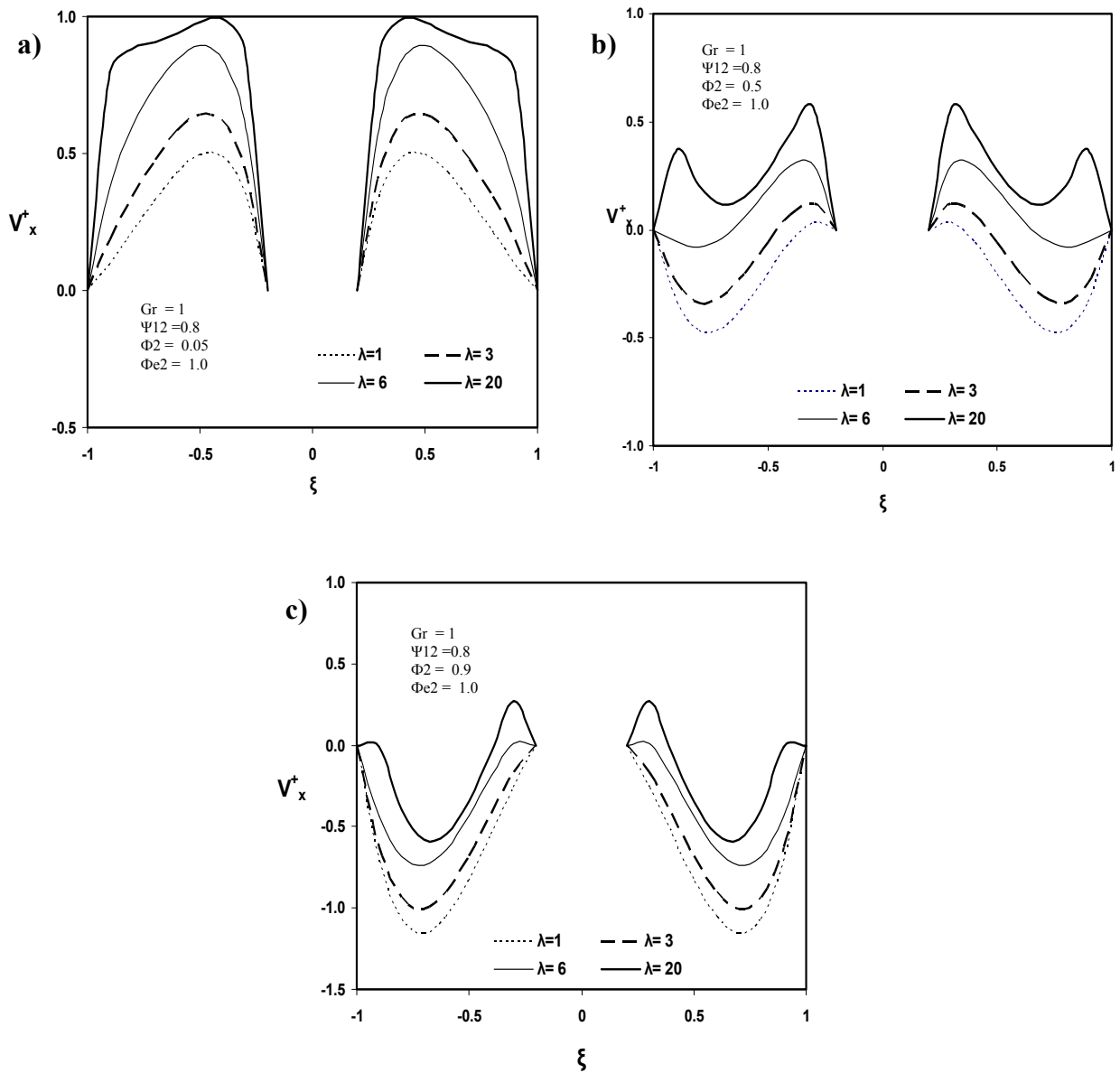


Figure 7.5 Typical hydrodynamic behavior of the physical system for Grashof number $Gr = 1$, electrical field in the axis direction, electrical potential ratio $\Psi_{12}=0.8$, and resistive heating effect $\phi_c^2 = 1.0$.

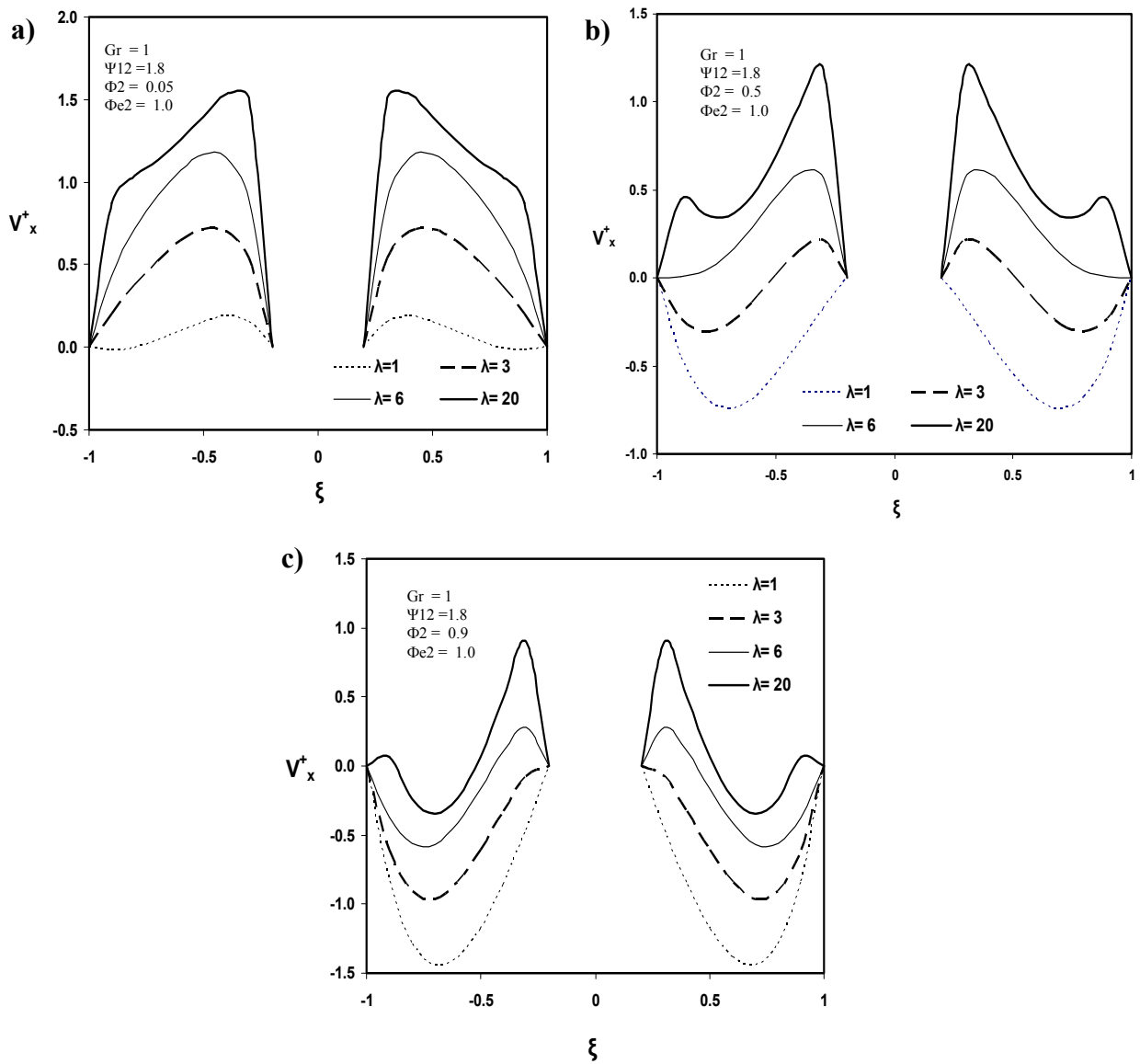


Figure 7.6 Typical hydrodynamic behavior of the physical system for Grashof number $Gr = 1$, electrical field in the axis direction, electrical potential ratio $\Psi_{12} = 1.8$, and resistive heating effect $\Phi_e = 1.0$.

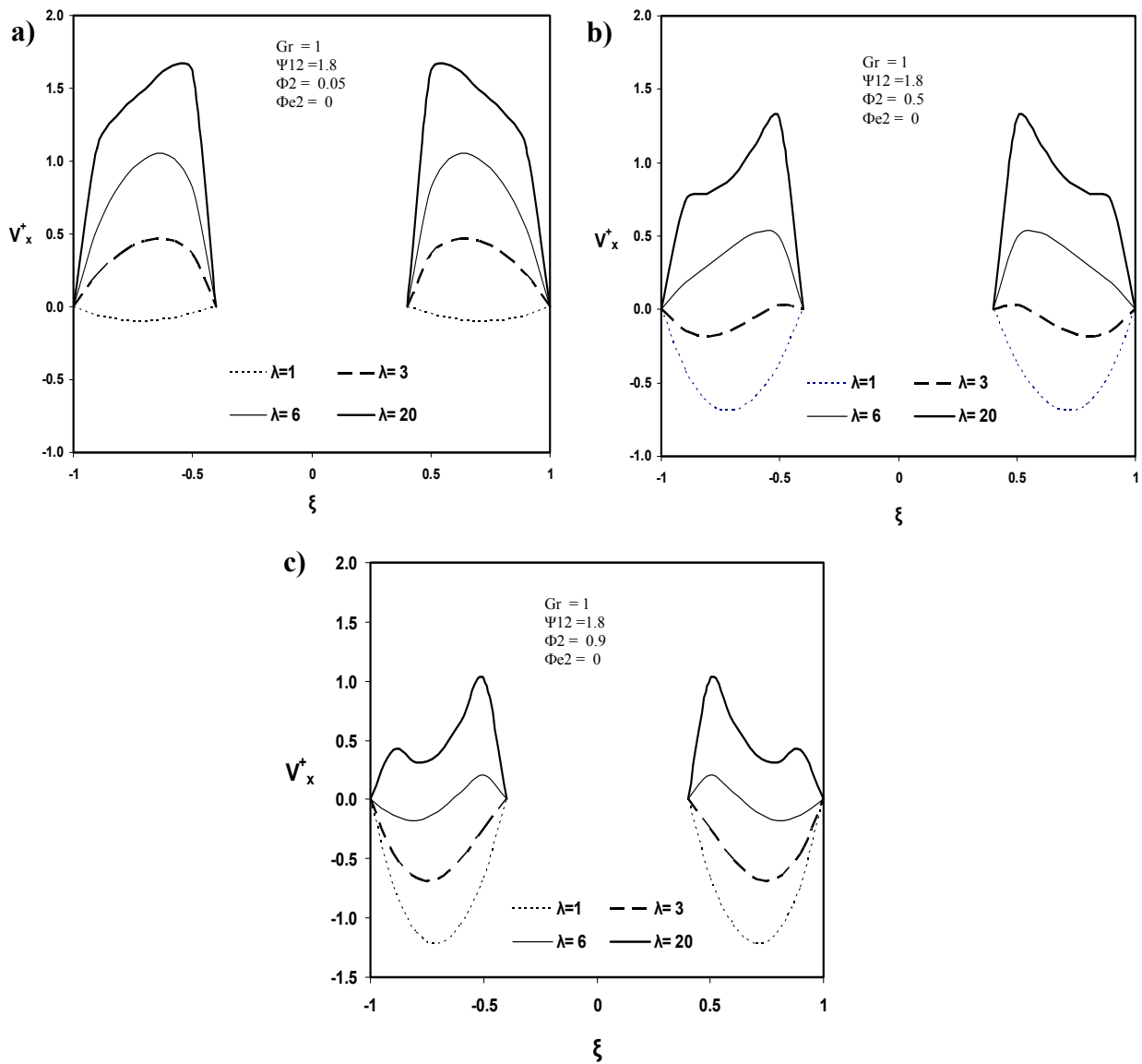


Figure 7.7 Typical hydrodynamic behavior of the physical system for Grashof number $Gr = 1$, electrical field in the axis direction, electrical potential ratio $\Psi_{12} = 1.8$, and no resistive heating effect $\phi_c = 0$.

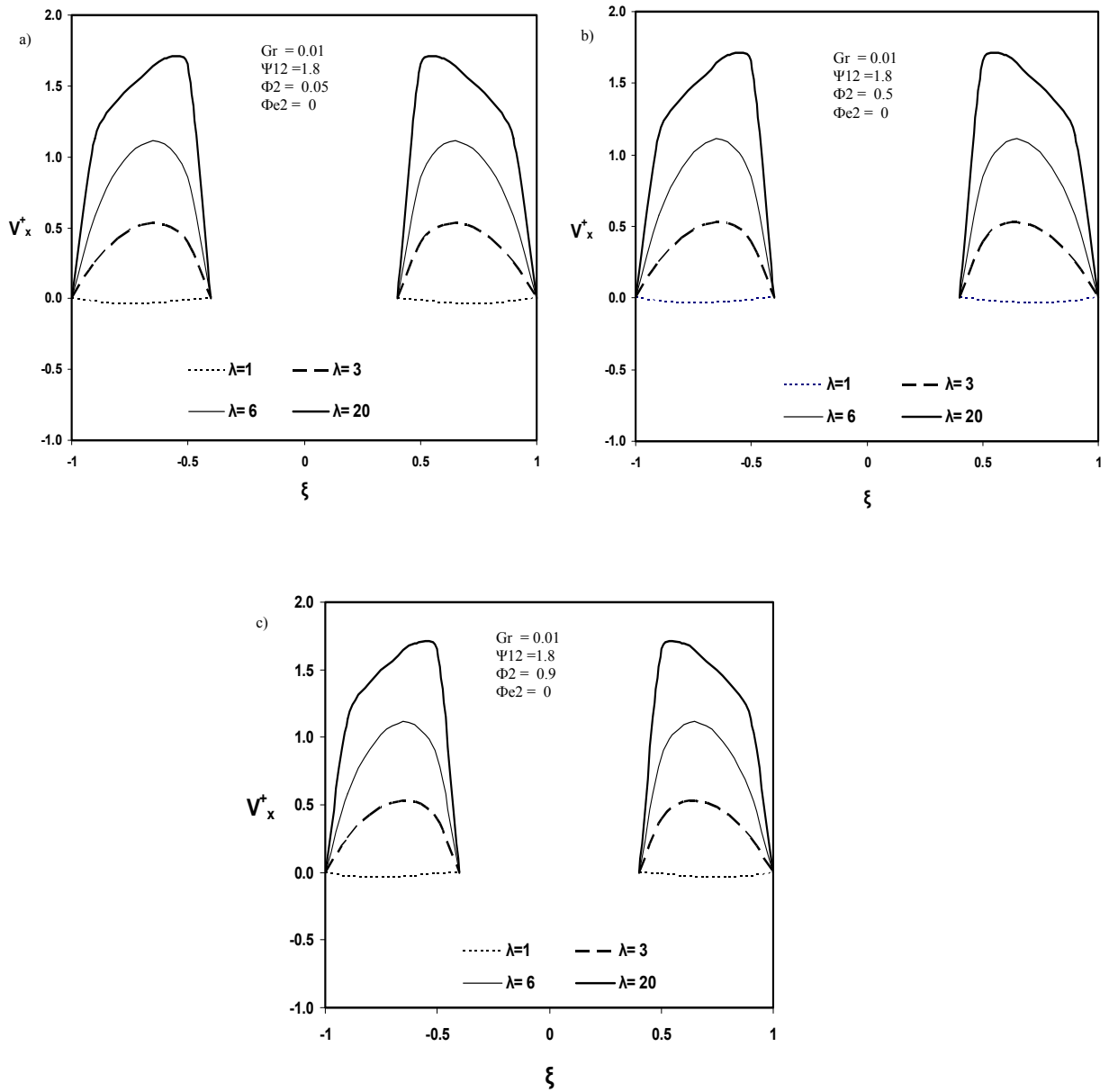


Figure 7.8 Typical hydrodynamic behavior of the physical system, for low influence of the buoyancy forces, Grashoff number $Gr = 10^{-2}$, electrical field in the axis direction, electrical potential ratio $\Psi_{12} = 1.8$, and no resistive heating effect $\Phi_e = 0$.

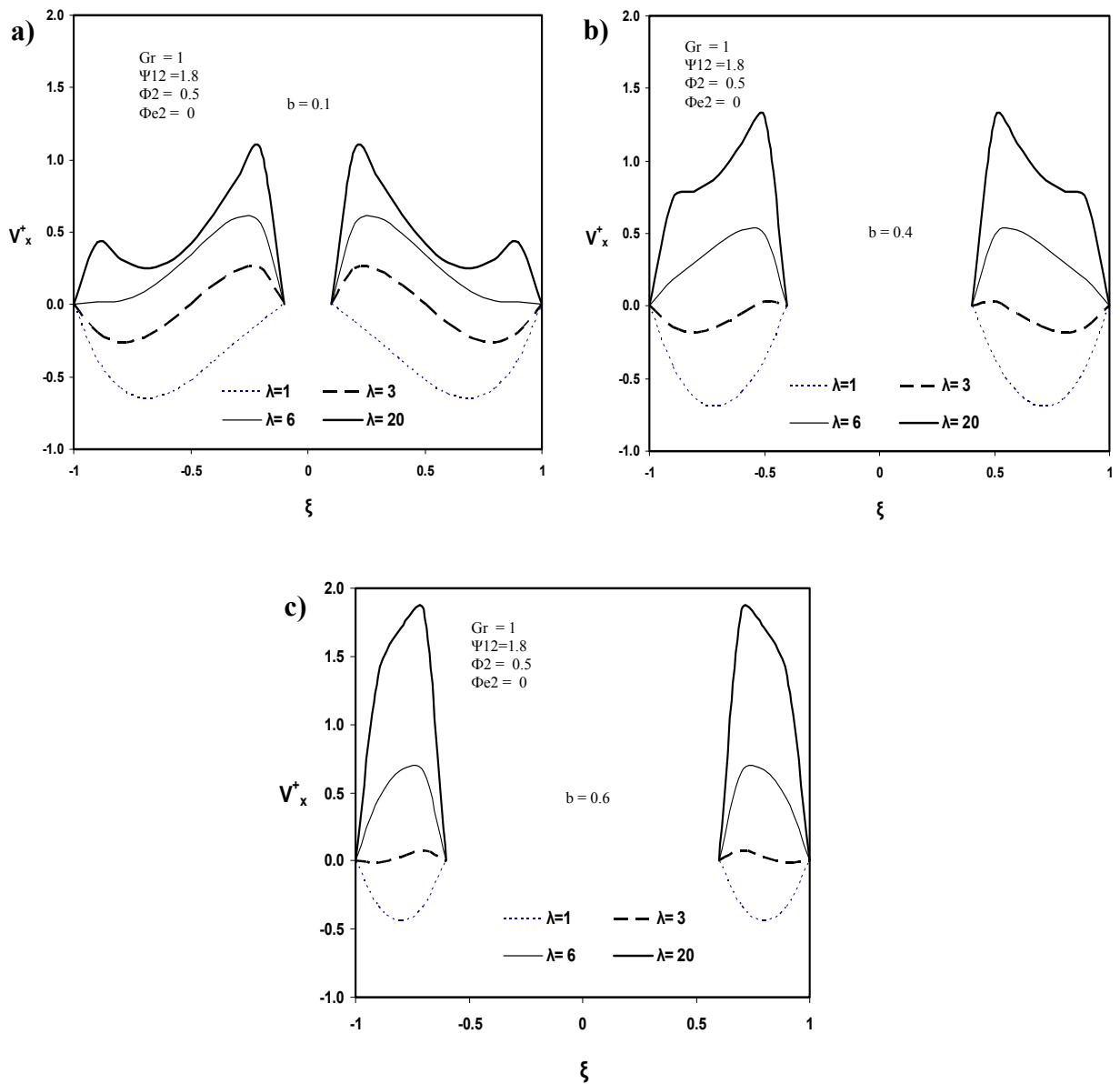


Figure 7.9 Typical hydrodynamic behavior of the physical system for Grashof number $Gr = 1$, electrical field in the axis direction, electrical potential ratio $\Psi_{12}=1.8$, Joule heating number $\phi_2=0.5$ and no resistive heating effect $\phi_c = 0$.

Figures 7.8 (a,b&c) present the same variables as in figures 7.7 (a,b&c) however the effect of buoyancy is attenuated or diminished for cases where the Grashoff number shows a lower value ($Gr = 0.01$). The set of figures show only a pressure-driven and an electroosmotic-driven family of flow regimes for all values of the Joule heating generation number. In the case of low inverse dimensionless Debye length parameter λ values (<2) the flow regime is pressure-driven while higher values cause only electroosmotic-driven flows.

Figure 7.9 (a,b&c) show velocity profiles for three cases of dimensionless core radius (b), respectively, and with the inverse dimensionless Debye length as a parameter. On this set of plots the Grashoff number, Gr , has been held at the value of unity, the electrical potential ratio, Ψ_{12} , held high (1.8) and the Joule heating number, ϕ^2 , held moderated (0.5). No resistive heating effect is considered in this set. Comparing figure 7.9 a,b&c for high λ values (>6), it is clearly observed that the tendency of flow regimes climbing the inner and outer walls completely disappear as porosity decreases. The end result is a complete electroosmotic dominated flow regime with maximum punctual velocity at the midway of the annular region. For a moderate λ value of 3, the original observed *flow reversal regime* is diminished as porosity decreases; however, it does not disappear. For low values of λ (≤ 1) a weaker pressure-driven flow is developed as porosity decreases.

7.5 Summary of the Chapter

The present chapter is the last in a series of three that study the hydrodynamic aspects yielded in a capillary channel. Above all, this chapter focuses on the analysis of hydrodynamic and its related issues using an annular geometry. The approach introduces an additional feature into the analysis; this is the porosity effect via the annular core. Considering this geometry, the different effects on flow regime caused by three competing forces have been simulated.

First, the scope and motivation are established in similar terms as in the previous two chapters. The quantitative and semi-quantitative description of the hydrodynamic taking place

in a porous media has been further extended to an annular capillary channel. This chapter in particular features the resistive characteristic of the annular core affecting temperature profile and fluid movement.

Second, the chapter describes the physical model and details of assumptions considered in an annular capillary channel. More complex theoretical equations are presented along with the corresponding solutions describing the system under study. Although in principle the cylindrical and annular geometries are the same in term of fundamental principles, this chapter gives emphasis to the main differences in the boundary conditions.

Finally, a complete set of illustrative results for the description of the system under study is presented. The analysis of the simulated portraits for flow regimes are analyzed in search for interpreting field test results.